Unforced interannual to decadal variability of global radiation imbalance: Role of low clouds

Ayumu Miyamoto,[a] Shang-Ping Xie,[a] , and Clara Deser[b]

[a] *Scripps Institution of Oceanography, University of California San Diego, La Jolla, California, USA*

[b] *National Center for Atmospheric Research, Boulder, Colorado, USA*

Revision submitted to Journal of Climate on March 1, 2026

Corresponding author: Ayumu Miyamoto, aymiyamoto@ucsd.edu

ABSTRACT: The global-mean radiation imbalance at the top of the atmosphere (GMTOA) is an important indicator of the climate response to anthropogenic greenhouse forcing. Natural variability perturbs this radiation imbalance on interannual and decadal timescales, confounding the externally forced signal. However, limited observations hinder efforts to understand the mechanisms of internally generated radiation imbalance. This study investigates the natural variability of global TOA radiation using a 500-year preindustrial coupled simulation with the Community Earth System Model version 2, and a corresponding atmospheric model simulation forced with daily sea surface temperature (SST) and sea ice from the coupled run. GMTOA variations lead those in tropical Pacific SST and global-mean surface temperature by 90° in phase, and are attributed to timescale-dependent SST patterns and associated low-cloud radiative effects. Interannual GMTOA peaks are driven by the development and decay of El Niño-Southern Oscillation (ENSO), which induce low-cloud anomalies that are maximized over the equatorial northeast Pacific. In contrast, decadal GMTOA variability stems from variations in eastern subtropical low cloud decks coupled with underlying SST anomalies. These low cloud-SST co-variations are triggered by stochastic extratropical atmospheric variability. This timescale dependence reflects the characteristics of these drivers: the amplitude of ENSO peaks at interannual timescales due to tropical ocean dynamics, whereas extratropical stochastic forcing on SST becomes increasingly important on decadal and longer timescales. Recent satellite observations of GMTOA corroborate both mechanisms. This study underscores the importance of subtropical low cloud-SST co-variations driven by extratropical atmospheric forcing in unforced variability of global energy imbalance.

1. Introduction

The Earth's energy budget is a fundamental physical property of the climate system, and governs the rise in global-mean surface temperature due to greenhouse gas forcing. The climate system responds to radiative forcing (F) at the top of the atmosphere (TOA) by modifying longwave emission and incoming solar radiation via changes in surface temperature. This global-mean energy budget may be cast as

$$N = F + \lambda T \tag{1}$$

where N is the net radiation (hereafter expressed as GMTOA; positive values for downward flux) and λ the climate feedback parameter which characterizes radiative feedback from perturbations in global-mean surface temperature (GMST) T (Gregory et al. 2004). Reducing uncertainty in projections of global warming is a pressing task for the climate research community. Radiative feedback estimates from historical changes $(N-F)/T$ have been extensively investigated to improve our understanding of and constraints on future warming (Sherwood et al. 2020).

In this context, decadal changes in GMTOA garner considerable attention. Satellite observations from Clouds and the Earth's Radiant Energy System (CERES) have yielded a continuous record of GMTOA for more than two decades (Loeb et al. 2024). The data record features a striking positive trend in planetary energy uptake, exceeding that simulated by global climate models (Raghuraman et al. 2021; Olonscheck and Rugenstein 2023). GMTOA and associated radiative feedbacks in the historical period are often estimated using atmospheric general circulation models (AGCMs) forced with observed sea surface temperature (SST) and sea ice, i.e., the AMIP (Atmospheric Model Intercomparison Project) protocol. The model simulations reveal substantial decadal variations in radiative feedbacks (Gregory and Andrews 2016; Andrews et al. 2018).

In addition to anthropogenic radiative forcing (e.g., CO_2, aerosols), natural variability needs to be considered in the historical variations of GMTOA (Dessler et al. 2018; Wills et al. 2021). For natural variability, the relationship between GMTOA and GMST is complex and distinct from the forced response. Their simultaneous correlation is nearly zero, and the peak correlation occurs with GMTOA leading by 45-90°, such that planetary heat uptake acts to raise GMST (Xie et al. 2016). The peak lagged correlation is modest on decadal timescales, implying the GMTOA variations are only loosely related to GMST.

This raises an important question: what causes natural decadal GMTOA variations? Almost in quadrature with each other (Xie et al. 2016), GMST is unlikely to be the major driver for GMTOA in natural variability. Instead, we show here that subtropical low clouds play an important role in the GMTOA variations. While tropical Pacific SST changes modulate subtropical low clouds through deep convective adjustment (Zhou et al. 2016), extratropical atmospheric variability and resultant eastern subtropical SST anomalies can locally drive the low cloud variations (Larson et al. 2024; Miyamoto and Xie 2025). Previous studies highlighted the tropical Pacific SST effect in relation to radiatively forced warming patterns—known as the pattern effect (e.g., Senior and Mitchell 2000; Dong et al. 2020; Andrews et al. 2022), but the subtropical SST effect has not been extensively examined.

The present study investigates unforced interannual to decadal variability of GMTOA based on a 500-year simulation under constant preindustrial radiative forcing with a state-of-the-art global climate model, Community Earth System Model version 2 (CESM2; Danabasoglu et al. 2020), and a corresponding "perfect-model" AMIP simulation forced with daily SST and sea ice from the coupled run. Unlike previous studies that examined GMTOA variations associated with GMST or selected SST modes (e.g., Xie et al. 2016; Wills et al. 2021), this study focuses on GMTOA itself without making any *a priori* assumptions about a relationship with SST modes. Our GMTOA-centric analysis reveals the regions and radiative components (cloud and clear-sky contributions) that are crucial in unforced GMTOA variability. The perfect AMIP run is utilized to disentangle stochastic atmospheric forcing and SST effects on the GMTOA variations. A comparison of interannual and decadal GMTOA variations aids the interpretation of the short CERES record.

The rest of the paper is organized as follows. Section 2 describes the data used in this study. Sections 3 and 4 document the natural GMTOA variability in CESM2 on interannual and decadal timescales, respectively. Section 5 compares the results with the recent CERES observations and discusses the timescale dependence. Section 6 concludes the paper with a summary of the key findings.

2. Data

a. Preindustrial simulations

We use a 500-year fully coupled CESM2 simulation with constant 1850-level radiative forcing (Danabasoglu et al. 2020; hereafter labeled CESM). Its atmosphere and ocean resolutions are nominally 1° in the horizontal with increasing meridional ocean resolution toward the equator. CESM2 simulates natural variability such as El Niño-Southern Oscillation (ENSO) and tropical Pacific decadal variability (TPDV) (Danabasoglu et al. 2020; Capotondi et al. 2020). The model also reproduces subtropical low clouds off the west coasts of continents (Fig. 1) and their positive feedback with underlying SST (Kang et al. 2023; Larson et al. 2024; Miyamoto and Xie 2025).

In parallel with the coupled run, a single-member AMIP simulation with identical boundary conditions (hereafter labeled CAM) was conducted by the CESM2 Climate Variability and Change Working Group (CVCWG). In this setup, the atmospheric component of CESM2, the Community Atmosphere Model version 6 (CAM6), is forced with daily SST and sea ice from CESM. This perfect-model/SST framework allows for a direct comparison with CESM (in a statistical sense owing to the limited ensemble size). If CAM fails to reproduce an anomaly of cloud, temperature, and wind in CESM, the anomaly can be attributed to stochastic atmospheric variability.

b. Observational data

For observational datasets, we use the Optimum Interpolation Sea Surface Temperature (OISST) version 2 (Huang et al. 2021) for SST, the CERES Energy Balanced and Filled edition 4.2 (Loeb et al. 2018) for radiative fluxes, the Moderate Resolution Imaging Spectroradiometer (MODIS) onboard Terra collection 6.1 (Platnick et al. 2003) for cloud cover, and the ERA5 global atmospheric reanalysis (Hersbach et al. 2020) for other meteorological variables. The horizontal resolution of the datasets is 0.25° for OISST and 1° for the others. For the MODIS low cloud cover, the random overlap assumption is applied to suppress the shielding effect of high clouds, as in Miyamoto and Xie (2025).

c. AMIP simulations with observed SST

In parallel with the CERES observations, we analyze two versions of AMIP simulations prescribed with observed SST and sea ice; one conducted by CVCWG uses CAM6 and the other

uses the Geophysical Fluid Dynamics Laboratory Atmospheric Model version 4 (AM4; Zhao et al. 2018). Hereafter, we refer to them as CAMobs and AMobs, respectively. The resolution of AM4 is approximately 100 km with 33 levels in the vertical. CAMobs covers the period 1880-2021, while AMobs covers 1982-2024. Both models are radiatively forced by historical forcing up to 2014 and Shared Socioeconomic Pathway scenarios (SSP3-7.0 for CAMobs and SSP2-4.5 for AMobs) from the Coupled Model Intercomparison Project phase 6 (Eyring et al. 2016). CAMobs uses the monthly-mean SST and sea ice from Extended Reconstructed SST version 5 (Huang et al. 2017) and OISST version 2, respectively, whereas AMobs uses daily-mean OISST version 2 for both SST and sea ice. Both models have 10 ensemble members each, and their ensemble averages are analyzed.

d. Preprocessing

All data are interpolated onto a 2.5° grid and smoothed with a 12-month running mean. Linear detrending is applied to all datasets unless otherwise noted. To decompose the anomalies into interannual and decadal components, a Lanczos filter with a cutoff period of 10 years was applied to the 500-year CESM and CAM simulations. For the decadal components, only calendar-year (January-to-December) 12-month averages are analyzed. The Lanczos time filtering was not applied because of the short observational record.

e. Statistical test

We assess the statistical significance of correlation and regression coefficients using a Student's t-test. To estimate the effective sample size, we calculate effective decorrelation time T_e following Metz (1991):

$$T_e = 1 + 2\sum_{\tau=1}^{L}\left(1-\frac{\tau}{L}\right)R_{XX}(\tau)R_{YY}(\tau). \tag{2}$$

$R_{XX}(\tau)$ and $R_{YY}(\tau)$ denote autocorrelation functions of variables X and Y at a lag of τ months/years. L is set to 120 months for interannual anomalies and 50 years for decadal anomalies. The effective sample size N_e is then given by

$$N_e = \frac{N_t}{T_e} \tag{3}$$

where N_t is the number of samples.

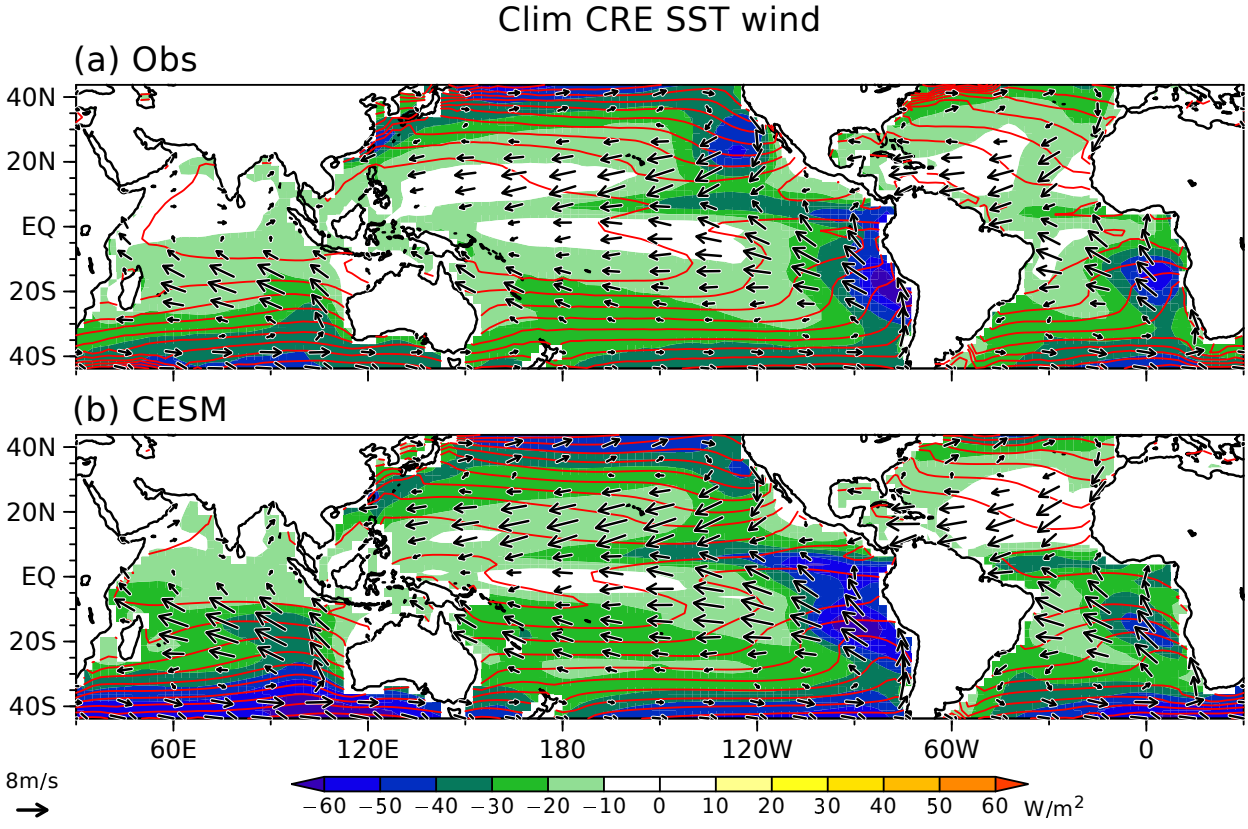

135 FIG. 1. Annual-mean climatology of SST (contoured for every 2 °C), surface wind (arrows; m s^{-1}), and TOA
136 cloud radiative effect (CRE; shading; W m^{-2}; positive values for heating) from (a) observations and (b) CESM.

3. Interannual variation

a. Lead-lag relationship

The correlation analysis indicates that GMTOA and GMST are in quadrature for both interannual and decadal variability in CESM (Fig. 2, top two rows). The lead of GMTOA over GMST in CESM is consistent with unforced variations in observations and other climate models, albeit the phase difference is somewhat larger than the multi-model mean (Xie et al. 2016; Lutsko and Takahashi 2018; Proistosescu et al. 2018). The GMTOA is highly correlated with the global net surface heat flux (Fig. S1), with the ocean absorbing 82% and 92% of the radiative energy input at lag 0 for interannual and decadal variability, respectively. The lagged relationship with GMST contrasts with forced climate change where radiative feedback is assumed to be proportional to GMST as in Eq. (1).

For interannual variability, the GMTOA is dominated by and closely tracks cloud radiative effect (CRE; Fig. 2h), while the upward clear-sky flux is nearly in phase with GMST (Fig. 2i). At the GMTOA peak, CRE, particularly its shortwave component, accounts for approximately 75%, with a secondary contribution from longwave clear-sky flux (Table 1). The weak concurrent anomalies in GMST and clear-sky fluxes suggest that natural GMTOA variability is not primarily driven by longwave damping on temperature variability (the Planck response or lapse rate feedback). This study therefore focuses on the cloud processes that create GMTOA anomalies under weak GMST anomalies.

Red lines in Figs. 2f-i indicate lag correlation of GMTOA between CESM and CAM, which assesses the SST effect on GMTOA and its lagged relationship in CESM. The autocorrelation of GMTOA in CESM is captured by CAM without significant lead-lag asymmetry (Fig. 2f). Reflecting the ability of CAM to capture the evolution of both CRE and clear-sky flux (Figs. 2h,i), the interannual correlation of GMTOA at lag 0 amounts to 0.71. Noting that single-member CAM has SST-unforced stochastic radiative noise unlike the ensemble-mean, this indicates that the ocean effect explains at least half of the CESM GMTOA variations. The strong ocean effect under weak GMST anomalies indicates the importance of the SST pattern.

TABLE 1. Global-mean TOA radiative flux (W m^{-2}) regressed onto GMTOA from CESM decadal, interannual, and CERES anomalies (left to right). In CESM decadal anomalies, values in parentheses indicate a +1-year lagged anomaly. SW and LW signify shortwave and longwave components, respectively. CLR denotes clear-sky flux. Boldface indicates statistical significance at the 90% confidence level.

	CESM decadal	CESM interannual	CERES
GMTOA	**0.12** (**0.11**)	**0.40**	**0.26**
Net CRE	**0.09** (**0.11**)	**0.29**	**0.19**
SW CRE	**0.09** (**0.11**)	**0.26**	**0.16**
LW CRE	0.00 (0.00)	**0.04**	0.02
Net CLR	**0.02** (0.00)	**0.11**	**0.07**
SW CLR	0.00 (0.01)	**0.03**	−0.02
LW CLR	0.02 (−0.01)	**0.08**	**0.09**

b. Spatial pattern

Figure 3 shows the time evolution of interannual radiation and surface temperature anomalies regressed onto GMTOA in CESM. At the GMTOA peak, positive net TOA anomalies are distributed across the tropics and part of the extratropical oceans (Fig. 3c). The strongest signal appears in the equatorial eastern Pacific with a secondary maximum in the Southeast Pacific. Over the Pacific, SST anomalies at lag 0 do not resemble any well-known SST modes of variability (Fig. 3d), but the lead-lag regression implies the effect of ENSO. In particular, the GMTOA peak is preceded by a La Niña signature (Fig. 3b) and followed by an El Niño pattern (Fig. 3f), consistent with previous studies (e.g., Lutsko and Takahashi 2018; Wills et al. 2021; Tsuchida et al. 2023). This link with the ENSO transition is confirmed by the high correlation (~ 0.7) between GMTOA and Niño-3.4 SST (5°S-5°N, 170°W-120°W) at lag ±9 months (Fig. 2j). At these lags, GMST is near its peak (Fig. 2g) consistent with the ENSO pacemaker effect on GMST (Kosaka and Xie 2013), while GMTOA is almost zero (Fig. 2f) due to offsetting anomalies over the Pacific and Indian Ocean (Figs. 3a,e).

c. Mechanism

The dominance of shortwave CRE in the GMTOA variations implies that low-level clouds play a crucial role through their albedo effect (Klein and Hartmann 1993). Figure 4 shows anomalies in low cloud cover and environmental controlling factors associated with interannual GMTOA

variations in CESM and CAM. Negative anomalies in low cloud cover are distributed across the tropical and extratropical oceans, leading to the increased shortwave energy uptake (Fig. 4a). This low-cloud decrease explains the TOA radiation changes well, with a pattern correlation of -0.83 between low cloud cover and net TOA radiation.

The decrease in tropical low clouds is accompanied by the weakening of lower tropospheric stability measured by Estimated Inversion Strength (EIS; Wood and Bretherton 2006) (Fig. 4c). This is largely due to zonally uniform tropical tropospheric cooling (Fig. 4g), a mechanism often invoked in previous literature on the SST pattern effect (Zhou et al. 2016; Fueglistaler 2019; Ceppi and Fueglistaler 2021). Following the moist adiabat set by SST in tropical ascent regions (Sobel et al. 2001), this cooling is driven by negative SST anomalies in the tropical Indo-Pacific and western Atlantic that remain after the La Niña peak (Figs. 3b,d,f,h; Enfield and Mayer 1997; Xie et al. 2009). Indeed, interannual GMTOA variations are positively correlated ($r = 0.52$; Fig. S2) with concurrent SST anomalies over the tropical ascent regions, which are measured by the SST$^{\#}$ index (the temperature of the warmest 30% minus the tropical average SST; Fueglistaler 2019). The pan-tropical cooling also induces a subsidiary positive effect on GMTOA through a reduction in clear-sky outgoing longwave emission (Fig. S3; Andrews and Webb 2018; Ceppi and Fueglistaler 2021). Low-cloud cover also decreases over the North Pacific, which is attributed to persistent SST cooling resulting from the weakening of the Aleutian Low during La Niña (Fig. 3b; Alexander et al. 2002; Yang et al. 2023). These results indicate the influence of decaying La Niña.

The developing El Niño drives the peak in TOA radiation anomalies over the equatorial eastern Pacific, which accounts for 23% of GMTOA (black box in Figs. 3c and 5b; 5% of Earth's surface). As shown in the magnified figure, the low cloud decrease peaks not along the equator but slightly to its north (Fig. 5b). Climatologically, the northward flow toward the intertropical convergence zone crosses a sharp SST gradient on the northern flank of the equatorial cold tongue, promoting stratus and shallow cumulus clouds there (Fig. 5a; Deser and Wallace 1990; Small et al. 2005). Consistent with this climatological-mean state, the changes in equatorial low clouds are associated with the emergence of a warmer cold tongue (Fig. 5e) in the developing El Niño (Fig. 3). This leads to anomalous warm-air advection to the north of the equator, which corresponds well with the decrease in low clouds (Fig. 5d). Thus, the developing El Niño plays a crucial role, in addition

to the decaying La Niña discussed in the previous paragraph. Similar SST and radiation patterns appear in the regression analysis against Niño-3.4 SST (Fig. S4).

In Fig. 4, corresponding anomalies in CAM are juxtaposed with the CESM results to examine the SST effect. CAM well reproduces the CESM pattern of low cloud anomalies despite its complexity (Fig. 4b). Combined with prescribed SST and simulated tropospheric temperature (Fig. 4h), CAM accurately captures the EIS anomalies (Fig. 4d). The anomalous warm advection due to warm SST anomalies in the eastern equatorial Pacific is also reproduced (Fig. 4f). These results corroborate the effect of ENSO-related SST anomalies on low clouds and therefore GMTOA.

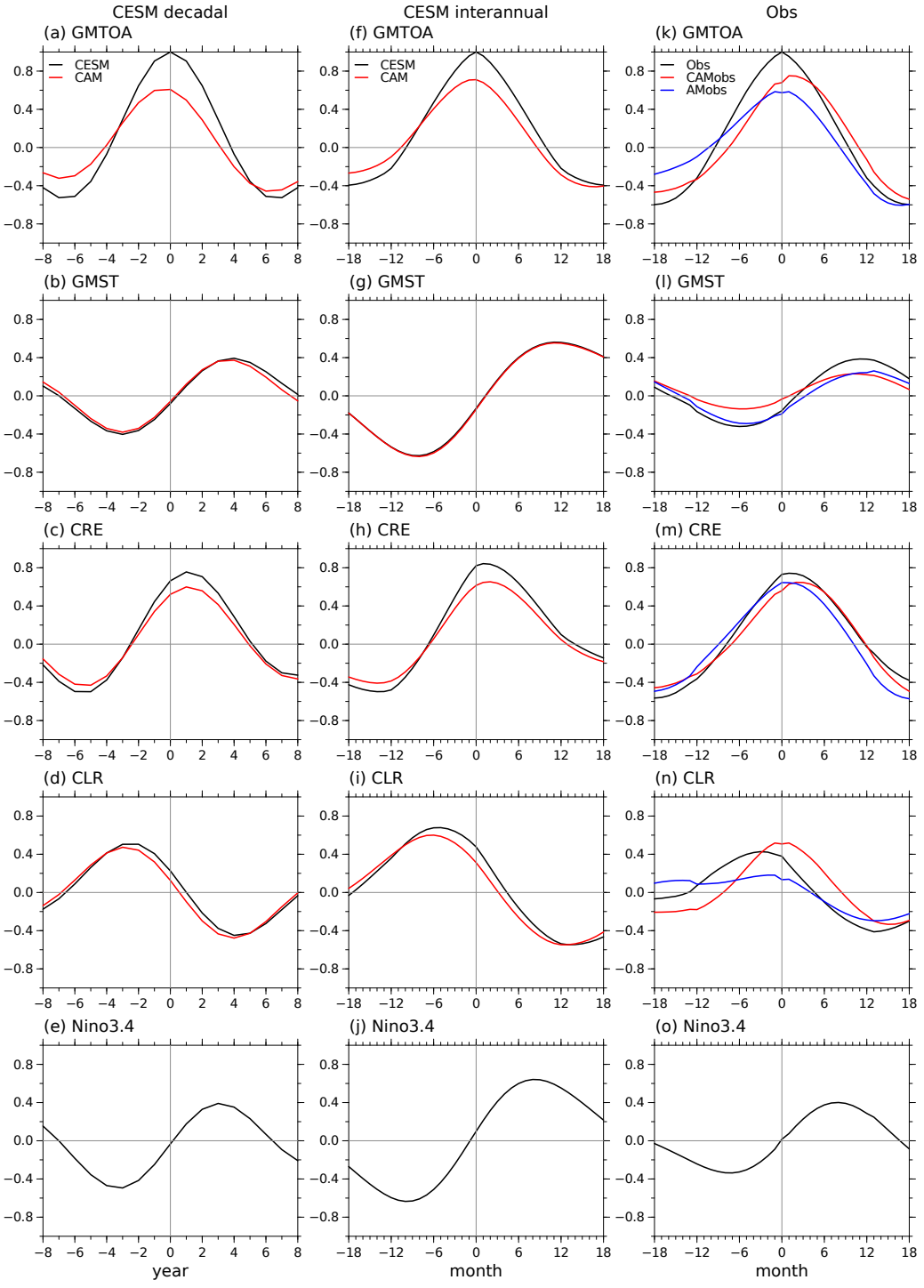

FIG. 2. Lead-lag correlation with GMTOA (positive values for heating) from (a-e) CESM decadal, (f-j) CESM interannual, and (k-o) observed anomalies (black lines). Colored lines denote the correlation of AMIP runs with CESM/CERES GMTOA. (a,f,k) GMTOA, (b,g,l) GMST, (c,h,m) global-mean CRE, (d,i,n) global-mean clear-sky flux, and (e,j,o) Niño-3.4 SST. Note that a positive lag means CESM/CERES GMTOA leads.

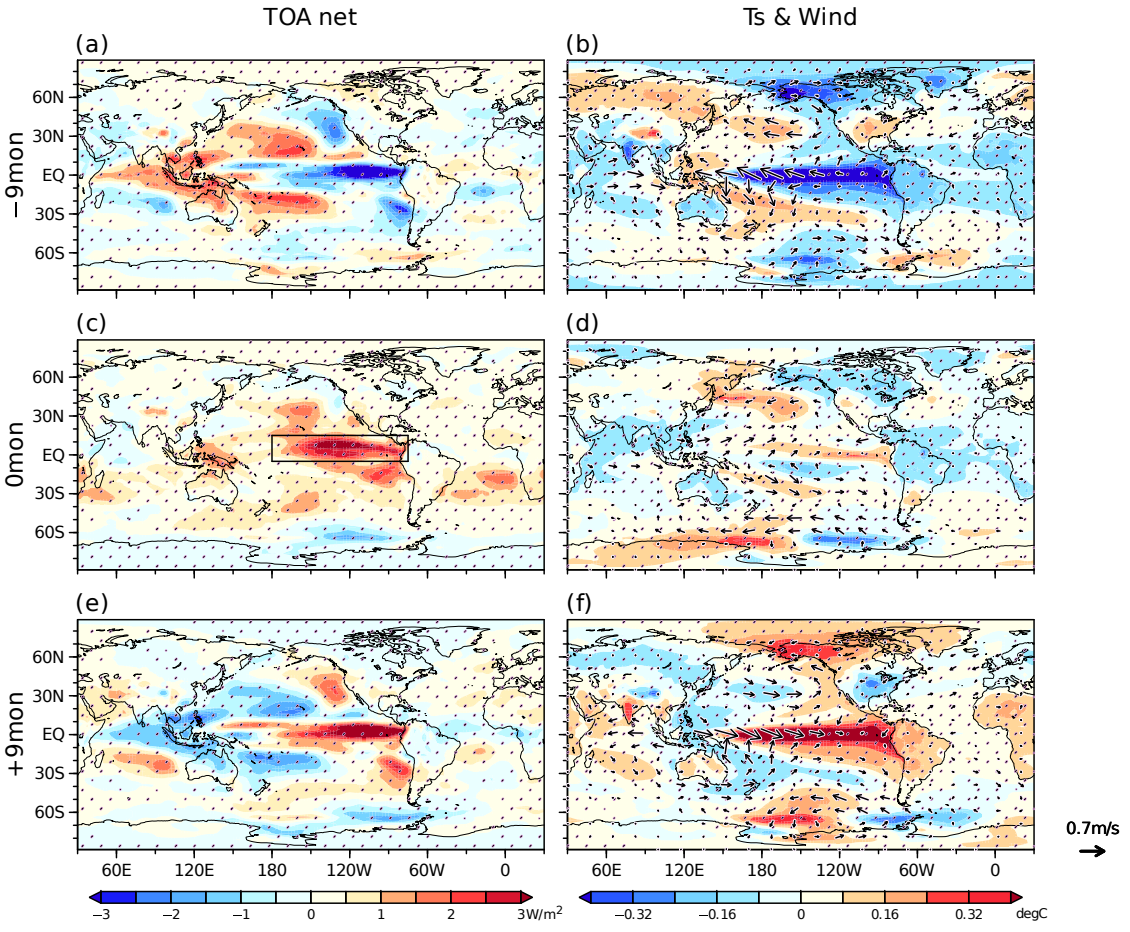

FIG. 3. Spatial pattern and time evolution of interannual GMTOA anomalies in CESM. Lagged regression maps of (a,c,e) TOA radiation (W m^{-2}), (b,d,f) surface temperature (shading; °C) and wind (arrows; m s^{-1}; only points with the 90% confidence are drawn) onto CESM interannual GMTOA anomalies at lags (a,b) −9, (c,d) 0, and (e,f) +9 months. Stippling indicates the 90% confidence. Lag-0 TOA radiation anomalies within black box explain 23% of GMTOA.

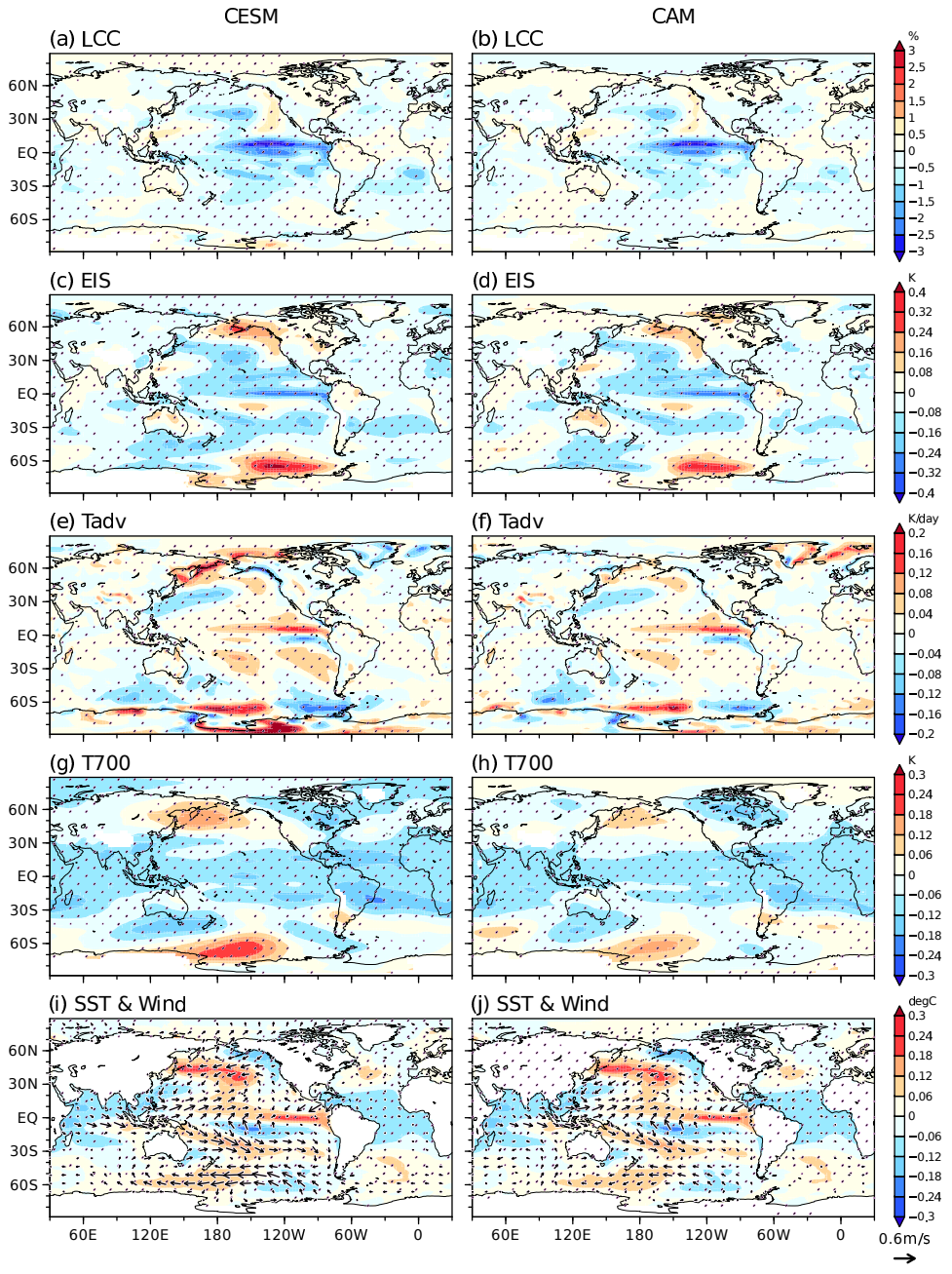

232 FIG. 4. Regression maps of (a,c,e,g,i) CESM and (b,d,f,h,j) CAM anomalies onto CESM interannual GMTOA
233 at lag 0. (a,b) Low cloud cover (%). (c,d) EIS (K). (e,f) surface temperature advection (K day^{-1}). (g,h) 700-hPa
234 temperature (K). (i,j) SST (shading; °C) and surface wind (arrows; m s^{-1}; only points with the 90% confidence
235 are drawn). Stippling indicates the 90% confidence.

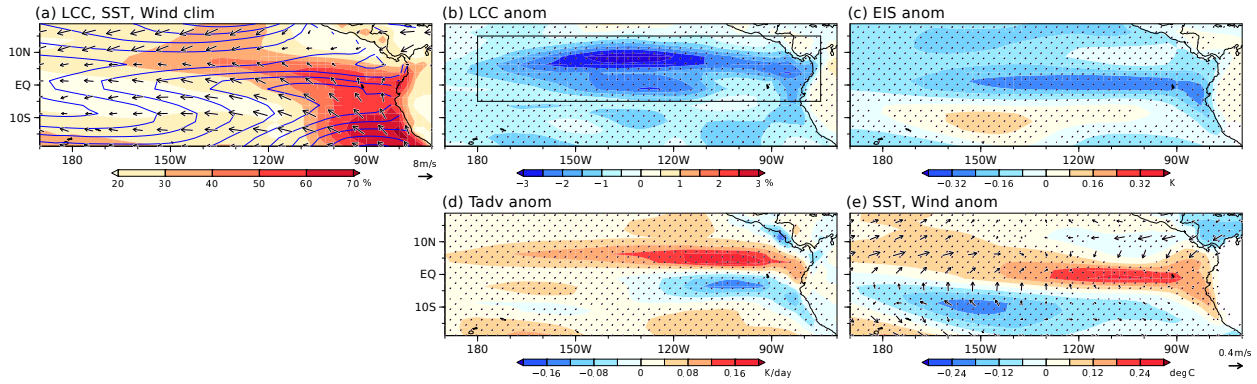

236 FIG. 5. (a) CESM climatology of low cloud cover (shading; %), SST (contoured for every 1 °C), and surface
237 winds (arrows, m s^{-1}). (b-d) magnified maps of Figs. 4a,c,e,i, respectively. Black box in (b) is the same as in
238 Fig. 3c.

4. Decadal variation

This section investigates the decadal GMTOA variability in CESM and contrasts it with the interannual counterpart. The lead-lag relationships on decadal timescales shown in Fig. 2a-d resemble those on interannual timescales. There is an approximately 90° phase-lagged relationship with GMST (black lines in Figs. 2a,b; Xie et al. 2016), with a weaker peak correlation compared to the interannual correlation. CRE accounts for 75% of the GMTOA peak through shortwave heating, compounded by a secondary clear-sky effect (Table 1). The peak in CRE emerges one year later (Fig. 2c), explaining nearly all the GMTOA anomaly (Table 1). As shown by the red lines in Figs. 2a-d, CAM reasonably captures these features, with a GMTOA correlation coefficient of 0.61 at lag 0 between CESM and CAM. While SST-unforced radiative noise is nonnegligible, this result underpins the quantitative importance of the ocean effect, with the SST pattern playing a key role under weak concurrent GMST anomalies.

a. Spatial pattern

Figure 6 shows the time evolution of radiation and surface temperature anomalies associated with the decadal GMTOA variations. Despite the similar temporal relationships on interannual and decadal timescales, there are marked differences in the spatial patterns of radiation. Remarkably, peak GMTOA on decadal timescales is associated with marked TOA radiation anomalies in the subtropical low-cloud regions (Figs. 6e,f). Strong positive signals occur over the Northeast Pacific and Southeast Indian Ocean, with a weaker signal over the South Atlantic. A positive signal in the eastern equatorial Pacific is much less dominant than on interannual timescales. The Southeast Pacific signal is not prominent at lag 0 but intensifies rapidly at lag +1, reaching a magnitude comparable to that in the North Pacific and Indian Ocean (Fig. 6g). These strong positive anomalies in the subtropical low cloud regions align with the peak of global-mean CRE (Fig. 2c).

As in the radiation anomalies, large SST anomalies at lag 0 and +1 years are confined to the eastern subtropical oceans (Figs. 6f,h). In contrast, the SST anomalies in the tropical ascending regions are very weak, as confirmed by negligible concurrent correlation with the $SST^{\#}$ index (Fig. S2). The pattern of concurrent SST and radiation anomalies contrasts sharply with its interannual counterpart. This difference implies that decadal GMTOA variability is not analogous to ENSO-driven variability, arising instead from fundamentally different physical processes.

It is noteworthy that the TPDV-like equatorial Pacific SST pattern transitions from a negative to a positive phase across lag 0 (Figs. 6b,j), although the maximum correlation between GMTOA and Niño-3.4 SST drops to 0.4 (Fig. 2e). At lag ±3 year when the TPDV-like SST signals are maximized, strong radiation changes over the Pacific tend to cancel out (Figs. 6a,i), as in the peak phase of ENSO (Figs. 6a,e). This spatial compensation in the peak phase of TPDV seems somewhat at odds with previous work claiming the equatorial Pacific warming pattern on global radiation (Zhou et al. 2016; Andrews and Webb 2018). This difference may reflect distinct global energy budgets governing natural variability and forced response.

b. Mechanism

Figure 7 shows anomalies in low cloud cover and environmental factors associated with decadal GMTOA variations in CESM and CAM. Here, lag +1-year fields are discussed to capture the rapid emergence of the Southeast Pacific signal and associated peak in global-mean CRE. Otherwise, the low-cloud signal is qualitatively the same as the lag-0 fields (Fig. S5). With a high spatial correlation of 0.88, the net radiation anomalies at lag +1 are well explained by anomalous low cloud decrease maximized over the Northeast Pacific, Southeast Pacific, and South Indian Ocean (Fig. 7a). The low cloud decrease is collocated with weakening of EIS (Fig. 7c). Although free-tropospheric cooling associated with decaying TPDV contributes to the low cloud decrease at lags −1 and 0 (Figs. S5,6), this signal is not obvious at lag 1 (Fig. 7g). Local SST warming strongly controls the decadal decrease of EIS and thus low clouds as positive low cloud-SST feedback (Fig. 7i). The low cloud-SST feedback through EIS corroborates CAM's reproducibility of the low cloud changes in CESM (Figs. 7b,d) and consequently GMTOA changes. The weakly opposing signal in the tropical Northeast Atlantic may be due to the lack of a pronounced low cloud deck there (Fig. 1). Similar to yet less dominant than the interannual variations, the decadal decrease in equatorial Pacific low clouds corresponds to the emergence of warm-phase TPDV (Figs. 7a,i).

The positive SST anomalies over the eastern subtropical oceans are accompanied by poleward wind anomalies embedded with anomalous extratropical circulations (Fig. 7i). These wind anomalies induce warm-air advection (Fig. 7e), suppressing turbulent heat loss from the ocean that, together with radiative heating due to the low cloud decrease, raises the SST (Table 2). Additionally, the warm advection directly reduces low cloud cover (Klein et al. 1995; Miyamoto

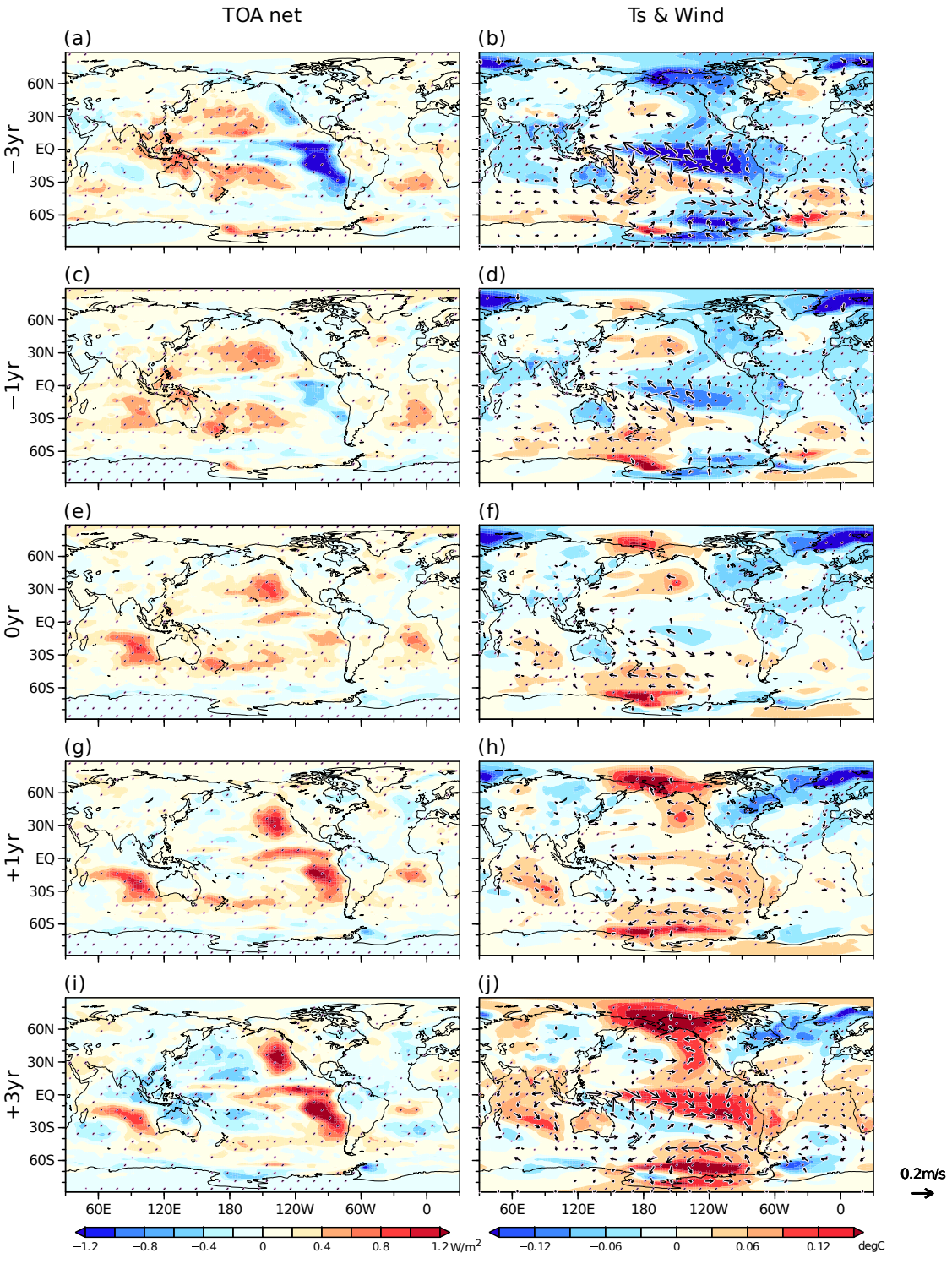

FIG. 6. As in Fig. 3, but for decadal anomalies. Lags (a,b) −3, (c,d) −1, (e,f) 0, (g,h) +1, (i,j) +3 years.

et al. 2018). The SST and wind anomalies extend westward and equatorward, indicative of the meridional modes (Chiang and Vimont 2004; Zhang et al. 2014) generated through wind-evaporation-SST (WES) feedback (Xie and Philander 1994). Recent studies have demonstrated that subtropical low cloud-SST feedback amplifies the meridional mode-like variability (Evan et al. 2013; Bellomo et al. 2014; Miyamoto et al. 2021, 2023; Kim et al. 2022). This result indicates that extratropical atmospheric variability drives the low cloud-SST co-variability and associated meridional modes.

A comparison of the wind anomalies between CESM and CAM reveals whether they are due to SST forcing or atmospheric internal variability (Figs. 7i versus 7j). While CAM partly captures the weakening of trade winds in WES feedback, it underestimates or even fails to simulate the extratropical circulation anomalies and associated poleward winds over the low cloud decks. This indicates that stochastic extratropical circulation variability triggers the low cloud-SST co-variability and meridional modes, thereby driving the GMTOA anomalies. Unlike SST-unforced radiative noise in a simple stochastic global energy budget model (Proistosescu et al. 2018), atmospheric internal variability affects GMTOA through changes in eastern subtropical SST.

In summary, decadal TOA radiation changes are dominated by subtropical low cloud decks, without prominent concurrent SST anomalies in the deep tropics. Extratropical stochastic variability makes a pronounced contribution to generating subtropical SST and low cloud anomalies. These SST anomalies, in turn, enable the AMIP to capture changes in GMTOA through low cloud-SST feedback. The dominance of the subtropical SST effect contrasts sharply with the interannual GMTOA variations.

TABLE 2. Lag +1-year area-average surface heat fluxes (Q_{net}=LH_a+LH_o+SH+SW+LW) regressed onto decadal GMTOA variability in CESM. Unit is W m^{-2} (positive values for downward flux). The averaging domains are shown in Fig. 7a. See Appendix for the latent heat flux decomposition.

	LH_a	SH	SW+LW	Q_{net}
North Pacific	0.17	0.03	0.41	0.32
South Indian Ocean	0.38	0.04	0.49	0.53
South Pacific	0.39	0.06	0.43	0.5

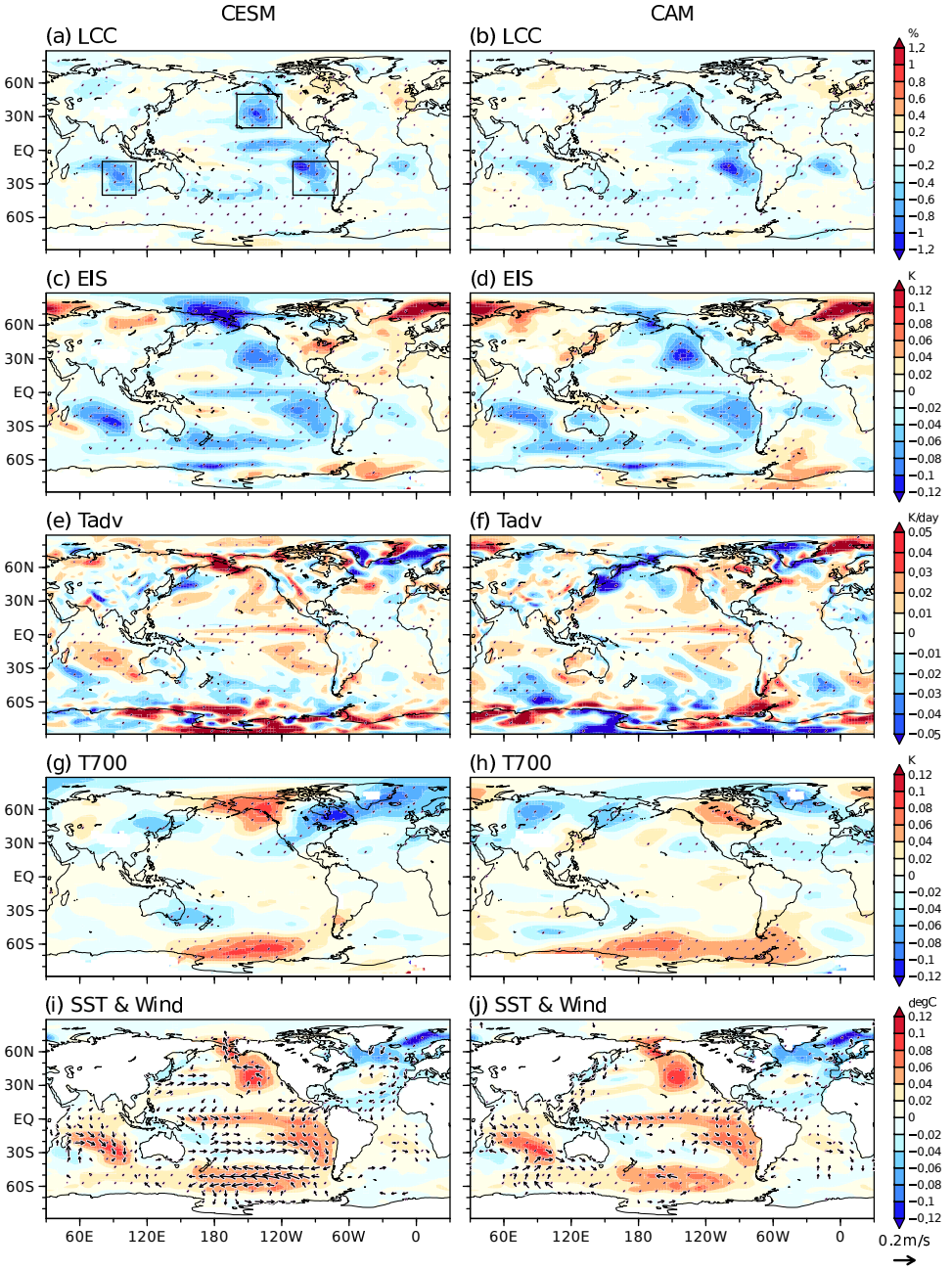

318 FIG. 7. As in Fig. 4, but for CESM decadal anomalies at lag +1 year. Black boxes in (a) indicate averaging
319 domains for Table 2.

5. Discussion

a. Comparison with CERES observations

Although short, the CERES observations serve as a valuable testbed to corroborate the findings from CESM. We analyze GMTOA variations in the CERES observations and the ensemble mean of two AMIP simulations (CAMobs and AMobs). Figure 8 shows time series of 12-month running-mean GMTOA. Although the two AMIPs underestimate the observed positive trend, they capture the interannual variations of GMTOA well, with correlations of $r = 0.68$ for CAMobs and 0.67 for AMobs based on detrended anomalies. AMobs reproduces the extreme GMTOA of 2022-2023 associated with the multi-year La Niña-El Niño transition (Tsuchida et al. 2026).

We repeat the same lead-lag analysis for the 21-year (2001-2021) detrended anomalies as for CESM. Despite the weaker lagged correlation with GMST, the observed lead-lag relationship of GMTOA and GMST is out-of-phase (Figs. 2k,l), aligned with the CESM result. Around the GMTOA peak, CRE dominates the GMTOA anomalies while the clear-sky effect is secondary (Figs. 2m,n and Table 1). The two AMIPs reproduce the observed GMTOA and CRE reasonably well (Figs. 2k,m), indicative of the SST effect.

The corresponding patterns of net radiation in the observations and AMIP simulations are shown in Figs. 9a-c. Both the observations and AMIPs feature increased incoming radiation over the equatorial eastern Pacific and subtropical Southeast Pacific accompanied by decrease in low clouds (Figs. 9d-f). Consistent with the emergence of ENSO discussed previously, positive SST anomalies appear along the equatorial Pacific (Fig. 9g) in the phase transition from La Niña to El Niño (Fig. 2o) accompanied by anomalous warm advection (Figs. S7d-f) and decreased EIS (Figs. S7a-c). Cooling in tropical tropospheric temperature is somehow inconsistent between observations and AMIPs (Figs. S7g-i), and its effect on GMTOA is unclear. The somewhat weaker relationship with ENSO in observations may reflect the short observational record, inclusion of decadal and forced changes, and excessively strong ENSO in CESM (Capotondi et al. 2020). We note that the maximum lagged correlation between GMTOA and Niño-3.4 SST increased from 0.4 to 0.5 when the CERES record is extended through 2024 to include the ENSO-induced extreme GMTOA of 2022-2023.

Positive TOA radiation anomalies over the subtropical Southeast Pacific correspond to a local rise in SST (Fig. 9g), suggestive of low cloud-SST feedback that is responsible for the AMIP reproducibility. The low cloud-SST co-variations are triggered by anomalous northwesterlies associated with extratropical cyclonic circulations (Fig. 9g). The AMIP simulations fail to reproduce the circulation pattern (Figs. 9h,i), indicating the predominance of stochastic atmospheric variability. Similar stochastically forced low cloud-SST feedback is found in the CESM interannual variations, where local maxima in net radiation and low cloud decrease over the Southeast Pacific (Figs. 3c and 4a) are accompanied by anomalous northwesterlies that are underestimated in CAM (Figs. 4i,j).

In summary, the CERES observations provide support for the contribution of ENSO and subtropical low cloud-SST feedback to GMTOA variations identified in CESM. A longer record is necessary to enhance the signal-to-noise ratio and isolate the decadal variability.

b. Relative roles of ENSO and extratropical atmospheric variability

This study highlights two drivers of distinct SST patterns responsible for GMTOA variations: ENSO and extratropical atmospheric variability. In CESM, the former dominates on interannual timescales, whereas the latter dominates on decadal timescales. It is not surprising that ENSO, the strongest natural mode of variability, plays a major role in GMTOA fluctuations. ENSO is essentially an interannual oscillation arising from redistribution of tropical ocean heat content (Jin 1997), with a period of 2-8 years in both observations and CESM2 (Capotondi et al. 2020). Meanwhile, SST variations driven by extratropical atmospheric forcing become more important on decadal and longer timescales through stochastic reddening (Hasselmann 1976). This diminishes the relative importance of equatorial Pacific-forced GMTOA variability on decadal timescales.

Still, decadal ENSO (or TPDV) has statistically significant lagged correlations with GMTOA (Figs. 2e and 6). In addition to forcing GMTOA, TPDV may be driven in part by extratropical atmospheric variability. Previous studies argued that subtropical Northeast and Southeast Pacific SST anomalies forced by atmospheric stochastic variability can modulate TPDV via Pacific meridional modes (Vimont 2005; Okumura 2013; Di Lorenzo et al. 2015; Sun and Okumura 2019). Indeed, such meridional mode-like patterns are found in the Pacific after the GMTOA peak (Figs. 6f,h,j). As the Pacific meridional mode is an important trigger of Central Pacific ENSO (Vimont

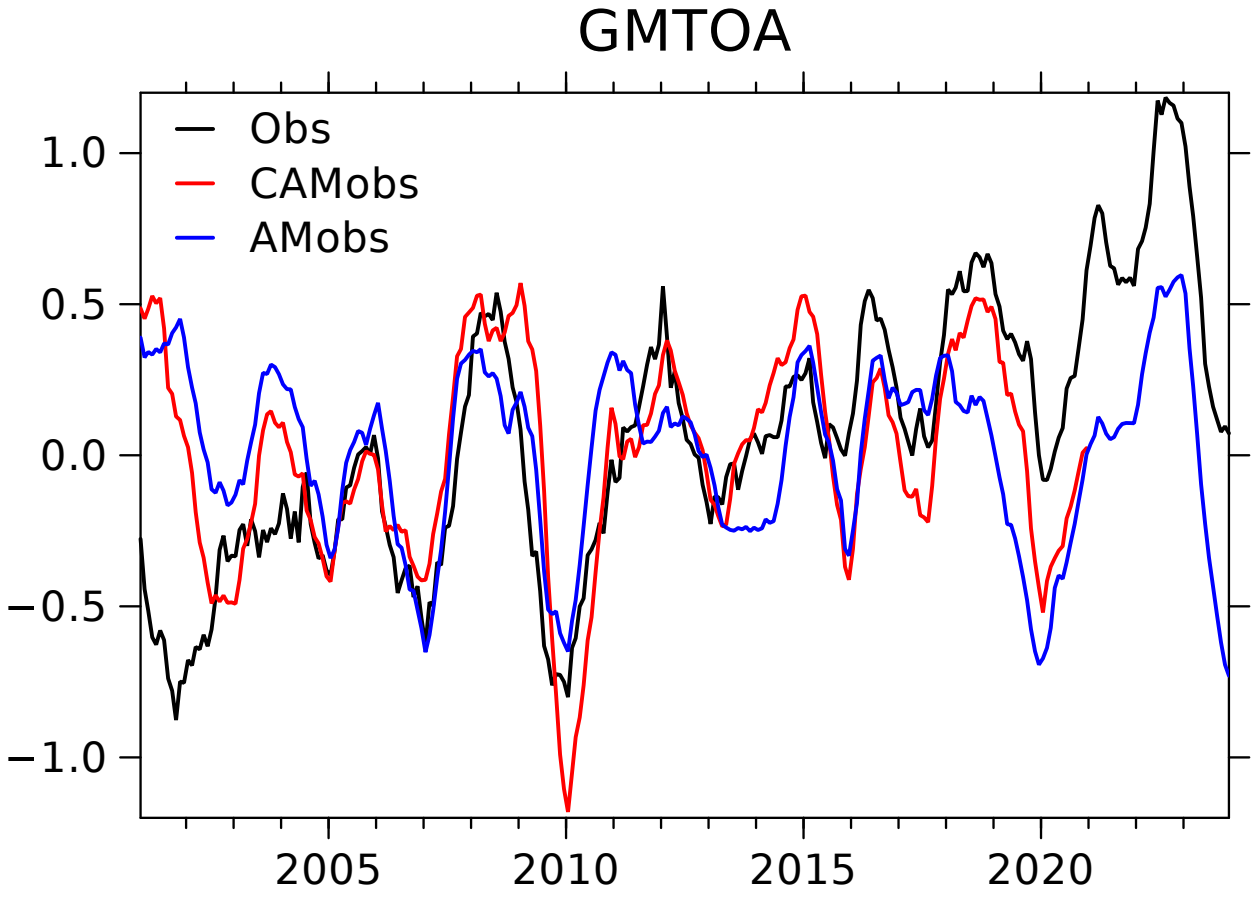

FIG. 8. Time series of non-detrended, 12-month running-mean GMTOA anomalies (W m^{-2}). Shown are CERES (black), AMobs (blue), and CAMobs (red; available through December 2021). Each value is plotted at the start of its respective 12-month window.

et al. 2014), extratropical atmospheric variability may also contribute to differences in radiative variability associated with canonical and Central Pacific ENSO. Further studies—say by using partially coupled runs—are needed to better understand the cause and effect of low cloud variability, particularly the relative contributions of tropical and extratropical forcings.

6. Conclusion

This study investigates the natural variability of GMTOA based on a 500-year CESM2 preindustrial simulation and a corresponding perfect-model AMIP simulation. We show that the GMTOA variations are attributed to low-cloud radiative effects driven by SST patterns that differ markedly between interannual and decadal timescales. This difference reflects the relative influence of two

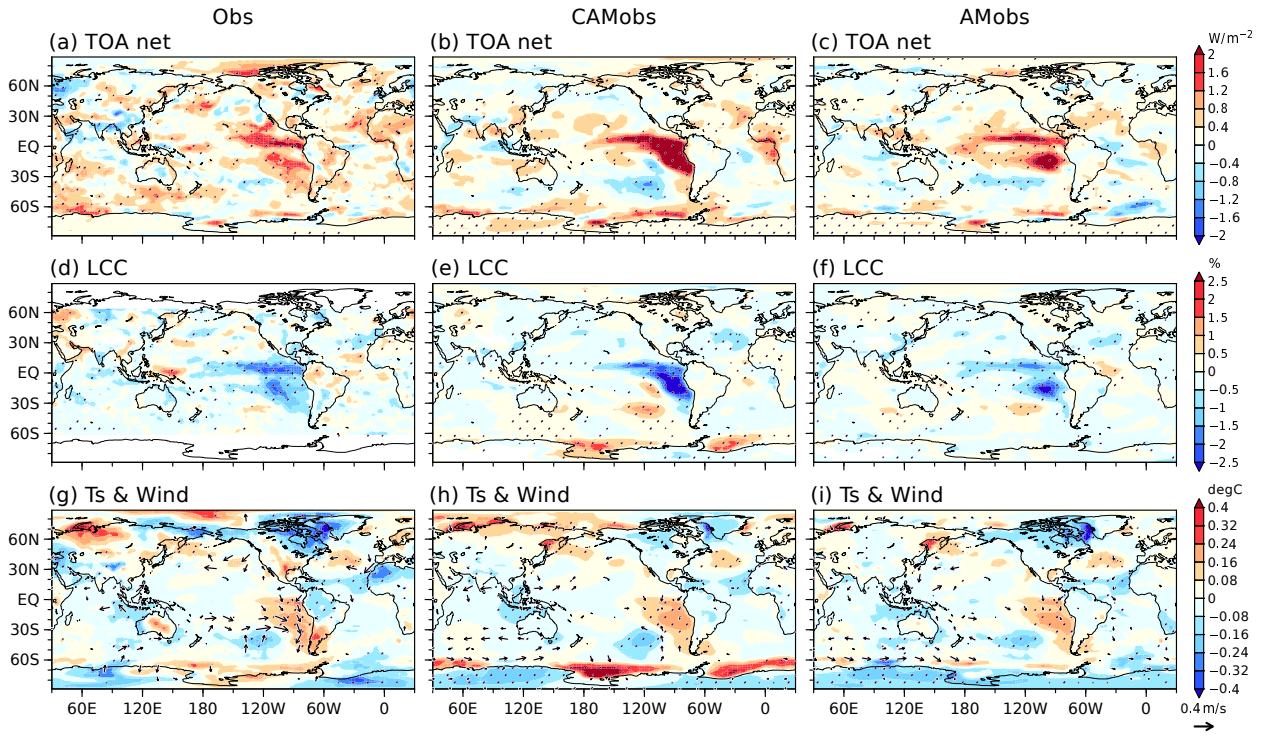

366 FIG. 9. Regression maps of (a,d,g) Observed, (b,e,h) CAMobs, and (c,f,i) AMobs anomalies onto CERES
367 GMTOA at lag 0. (a-c) TOA radiation (W m^{-2}). (d-f) Low cloud cover (%). (g-i) surface temperature (shading;
368 °C) and wind (arrows; m s^{-1}; only points with the 90% confidence are drawn). Stippling indicates the 90%
369 confidence.

396 distinct drivers: ENSO on interannual timescales and eastern subtropical SST forced by extratropi-
397 cal atmospheric variability on decadal timescales. The CERES observations support the influence
398 of both drivers on GMTOA.

399 On interannual timescales, low cloud anomalies are distributed across tropical and extratropical
400 oceans, with maxima over the equatorial eastern Pacific in the transition phase of ENSO. During
401 positive GMTOA anomalies, reduced low cloud cover over the northeastern equatorial Pacific
402 arises from anomalous warm advection due to a developing El Niño. Meanwhile, the remaining
403 broad decrease in low clouds aligns with weakened stability primarily during the decaying phase
404 of La Niña, which leaves an imprint on free-troposphere temperature and SST nonlocally through
405 teleconnections. In contrast, decadal GMTOA variability features more localized radiation anoma-
406 lies in the eastern subtropical low cloud decks without concurrent SST changes in the deep tropics.

These cloud anomalies are collocated with underlying SST anomalies, which allow AMIPs to reproduce the CRE changes through low cloud-SST feedback. The low cloud-SST co-variations are triggered by stochastic wind anomalies associated with extratropical atmospheric variability. This timescale dependence likely reflects the nature of these drivers: ENSO peaks on interannual timescales due to tropical ocean dynamics, while extratropical atmospheric forcing on SST becomes increasingly important on longer timescales. This study for the first time emphasizes the importance of the extratropical-forced subtropical low cloud-SST variations on GMTOA.

This study demonstrates the importance of SST patterns for GMTOA through a perfect model framework. In the unforced pattern effect, low cloud anomalies are driven not only by equatorial Pacific SST but also by stochastically forced eastern subtropical SST. As ENSO and TPDV can also drive the low cloud-SST variations (Yang et al. 2023), it remains challenging to assess their relative contributions only by using AMIP simulations forced with regional SST anomalies, e.g., the Green's function approach (Zhou et al. 2017; Bloch-Johnson et al. 2024). To address this, ocean-atmosphere coupled modeling or advanced statistical techniques are likely to be required.

We find that the spatial pattern of TOA radiation anomalies associated with GMTOA variability markedly differs from that associated with GMST variability, which is characterized by pronounced signals in the equatorial Pacific and high latitudes (Kosaka and Xie 2013; Xie et al. 2016; Deser et al. 2017). This discrepancy implies a redistribution of heat by atmospheric and oceanic circulations. The energy input may not only be passively advected but interact with the circulations. One plausible mechanism inferred from the decadal variations is that anomalous heat uptake in the North and South Pacific may propagate equatorward via the joint low cloud-WES feedback (Bellomo et al. 2014; Kim et al. 2022; Miyamoto et al. 2023) and subsurface ocean adjustment (Luongo et al. 2025), potentially modulating TPDV and consequently GMST. The role of coupled dynamics in linking global energy imbalance to temperature patterns warrants further investigation.

CERES data reveal a marked positive trend of GMTOA over the past two decades. The associated SST warming is pronounced in the Northeast Pacific, the South Indian Ocean, and the South Atlantic (Fig. 4 in Loeb et al. 2024). This pattern bears some resemblance to that of the unforced GMTOA variations identified in this study. Given the importance of subtropical low clouds in both forced and unforced GMTOA variability, it is essential to carefully attribute the observed changes.

Although partially supported by the observational datasets, this study is primarily based on a single model and subject to model uncertainties. This study shows how ENSO and eastern subtropical SST variations affect GMTOA through changes in low clouds. Inter-model differences in these processes may contribute to the spread in GMTOA variations, including the phase lag with GMST (Tsuchida et al. 2023). The representation of low clouds (e.g., low cloud-SST feedback) remains a challenge for climate models (Myers et al. 2021; Kim et al. 2022; Kang et al. 2023). In addition to its role in forced climate feedback (Zelinka et al. 2020), its improvement is key to narrowing the inter-model spread in unforced GMTOA variability. Addressing these biases will ultimately help us understand the historical GMTOA variations and constrain future warming.

Acknowledgments. We thank Prof. Dan Vimont and two anonymous reviewers for their constructive comments that greatly improved the manuscript. We thank Dr. Isla Simpson for setting up the perfect-model CAM6 simulation and CESM CVCWG for making CESM2/CAM6 simulations publicly available. A.M. and S.-P.X. were supported by the National Science Foundation (NSF, AGS 2105654). The Japanese Ministry of Education, Culture, Sports, Science and Technology (MEXT) program for the advanced studies of climate change projection (JPMXD0722680395) provided the computational resources for the AM4 simulation. The National Center for Atmospheric Research (NCAR) is sponsored by the NSF under Cooperative Agreement 1852977.

Data availability statement. The observational data used in this study are available online (ERA5: `https://cds.climate.copernicus.eu`; CERES-EBAF: `https://ceres.larc.nasa.gov/data`; MODIS: `https://ladsweb.modaps.eosdis.nasa.gov/archive/allData/61/MOD08_D3`; OISST: `https://psl.noaa.gov/data/gridded/data.noaa.oisst.v2.highres.html`). CESM2 and CAM6 simulations were downloaded from the casper system in National Center for Atmospheric Research. The authors can provide AM4 experiments upon reasonable requests.

APPENDIX

Decomposition of surface heat flux

Anomalous surface heat flux can be decomposed into latent heat (LH), sensible heat (SH), shortwave (SW), and longwave (LW) components. LH is a mixture of atmosphere-driven and SST-damping components. Following Xie et al. (2010), the SST damping term may be cast as

$$\mathrm{LH}'_{\mathrm{o}} = \overline{\mathrm{LH}} \left(\frac{1}{\overline{q_s}} \frac{\mathrm{d}\overline{q_s}}{\mathrm{d}T_a} \right) \mathrm{SST}' \tag{A1}$$

where T_a and q_s are air temperature and saturation specific humidity following the Clausius-Clapeyron equation, respectively. Overbar and prime denote monthly climatology and anomaly, respectively. The residual of anomalous latent heat flux represents the atmosphere-driven component ($\mathrm{LH}'_{\mathrm{a}}$) related to anomalous atmospheric conditions,

$$\mathrm{LH}'_{\mathrm{a}} = \mathrm{LH}' - \mathrm{LH}'_{\mathrm{o}}. \tag{A2}$$

References

Alexander, M. A., I. Bladé, M. Newman, J. R. Lanzante, N.-C. Lau, and J. D. Scott, 2002: The atmospheric bridge: The influence of ENSO teleconnections on air-sea interaction over the global oceans. *J. Climate*, **15**, 2205–2231, https://doi.org/10.1175/1520-0442(2002)015⟨2205:TABTIO⟩2.0.CO;2.

Andrews, T., and Coauthors, 2022: On the effect of historical SST patterns on radiative feedback. *J. Geophys. Res.*, **127**, e2022JD036675, https://doi.org/10.1029/2022JD036675.

Andrews, T., and M. J. Webb, 2018: The dependence of global cloud and lapse rate feedbacks on the spatial structure of tropical Pacific warming. *J. Climate*, **31**, 641–654, https://doi.org/10.1175/JCLI-D-17-0087.1.

Andrews, T., and Coauthors, 2018: Accounting for changing temperature patterns increases historical estimates of climate sensitivity. *Geophys. Res. Lett.*, **45**, 8490–8499, https://doi.org/10.1029/2018GL078887.

Bellomo, K., A. Clement, T. Mauritsen, and B. Stevens, 2014: Simulating the role of subtropical stratocumulus clouds in driving Pacific climate variability. *J. Climate*, **27**, 5119–5131, https://doi.org/10.1175/JCLI-D-13-00548.1.

Bloch-Johnson, J., and Coauthors, 2024: The Green's function model intercomparison project (GFMIP) protocol. *J. Adv. Model. Earth Syst.*, **16**, e2023MS003700, https://doi.org/10.1029/2023MS003700.

Capotondi, A., C. Deser, A. S. Phillips, Y. M. Okumura, and S. M. Larson, 2020: ENSO and Pacific Decadal Variability in the Community Earth System Model version 2. *J. Adv. Model. Earth Syst.*, **12**, e2019MS002022, https://doi.org/10.1029/2019MS002022.

Ceppi, P., and S. Fueglistaler, 2021: The El Niño-Southern Oscillation pattern effect. *Geophys. Res. Lett.*, **48**, e2021GL095261, https://doi.org/10.1029/2021GL095261.

Chiang, J. C. H., and D. J. Vimont, 2004: Analogous Pacific and Atlantic meridional modes of tropical atmosphere-ocean variability. *J. Climate*, **17**, 4143–4158, https://doi.org/10.1175/JCLI4953.1.

Danabasoglu, G., and Coauthors, 2020: The community earth system model version 2 (CESM2). *J. Adv. Model. Earth Syst.*, **12**, e2019MS001916, https://doi.org/10.1029/2019MS001916.

Deser, C., R. Guo, and F. Lehner, 2017: The relative contributions of tropical Pacific sea surface temperatures and atmospheric internal variability to the recent global warming hiatus. *Geophys. Res. Lett.*, **44**, 7945–7954, https://doi.org/10.1002/2017GL074273.

Deser, C., and J. M. Wallace, 1990: Large-scale atmospheric circulation features of warm and cold episodes in the tropical Pacific. *J. Climate*, **3**, 1254–1281, https://doi.org/10.1175/1520-0442(1990)003⟨1254:LSACFO⟩2.0.CO;2.

Dessler, A. E., T. Mauritsen, and B. Stevens, 2018: The influence of internal variability on Earth's energy balance framework and implications for estimating climate sensitivity. *Atmos. Chem. Phys.*, **18**, 5147–5155, https://doi.org/10.5194/acp-18-5147-2018.

Di Lorenzo, E., G. Liguori, N. Schneider, J. C. Furtado, B. T. Anderson, and M. A. Alexander, 2015: ENSO and meridional modes: A null hypothesis for Pacific climate variability. *Geophys. Res. Lett.*, **42**, 9440–9448, https://doi.org/10.1002/2015GL066281.

Dong, Y., K. C. Armour, M. D. Zelinka, C. Proistosescu, D. S. Battisti, C. Zhou, and T. Andrews, 2020: Inter-model spread in the sea-surface temperature pattern effect and its contribution to climate sensitivity in CMIP5 and CMIP6 models. *J. Climate*, **33**, 7755–7775, https://doi.org/10.1175/JCLI-D-19-1011.1.

Enfield, D. B., and D. A. Mayer, 1997: Tropical Atlantic sea surface temperature variability and its relation to El Niño-Southern Oscillation. *J. Geophys. Res.*, **102**, 929–945, https://doi.org/10.1029/96JC03296.

Evan, A. T., R. Allen, R. Bennartz, and D. J. Vimont, 2013: The modification of sea surface temperature anomaly linear damping time scales by stratocumulus clouds. *J. Climate*, **26**, 3619–3630, https://doi.org/10.1175/JCLI-D-12-00370.1.

Eyring, V., S. Bony, G. A. Meehl, C. A. Senior, B. Stevens, R. J. Stouffer, and K. E. Taylor, 2016: Overview of the Coupled Model Intercomparison Project phase 6 (CMIP6) experimental design and organization. *Geoscientific Model Development*, **9**, 1937–1958, https://doi.org/10.5194/gmd-9-1937-2016.

Fueglistaler, S., 2019: Observational evidence for two modes of coupling between sea surface temperatures, tropospheric temperature profile, and shortwave cloud radiative effect in the tropics. *Geophys. Res. Lett.*, **46**, 9890–9898, https://doi.org/10.1029/2019GL083990.

Gregory, J., and Coauthors, 2004: A new method for diagnosing radiative forcing and climate sensitivity. *Geophys. Res. Lett.*, **31**, L03205, https://doi.org/10.1029/2003GL018747.

Gregory, J. M., and T. Andrews, 2016: Variation in climate sensitivity and feedback parameters during the historical period. *Geophys. Res. Lett.*, **43**, 3911–3920, https://doi.org/10.1002/2016GL068406.

Hasselmann, K., 1976: Stochastic climate models Part I. Theory. *Tellus*, **28**, 473–485, https://doi.org/10.1111/j.2153-3490.1976.tb00696.x.

Hersbach, H., and Coauthors, 2020: The ERA5 global reanalysis. *Quart. J. Roy. Meteor. Soc.*, **146**, 1999–2049, https://doi.org/10.1002/qj.3803.

Huang, B., P. W. Thorne, V. F. Banzon, T. Boyer, G. Chepurin, and J. H. Lawrimore, 2017: Extended reconstructed sea surface temperature, version 5 (ERSSTv5): Upgrades, validations, and intercomparisons. *J. Climate*, **30**, 8179–8205, https://doi.org/10.1175/JCLI-D-16-0836.1.

Jin, F.-F., 1997: An equatorial ocean recharge paradigm for ENSO. Part 1: Conceptual model. *J. Atmos. Sci.*, **54**, 811–829, https://doi.org/10.1175/1520-0469(1997)054⟨0811:AEORPF⟩2.0.CO;2.

Kang, S. M., P. Ceppi, Y. Yu, and I.-S. Kang, 2023: Recent global climate feedback controlled by Southern Ocean cooling. *Nat. Geosci.*, **16**, 775–780, https://doi.org/10.1038/s41561-023-01256-6.

Kim, H., S. M. Kang, J. E. Kay, and S.-P. Xie, 2022: Subtropical clouds key to Southern Ocean teleconnections to the tropical Pacific. *Proc. Natl. Acad. Sci. (USA)*, **119**, e2200514119, https://doi.org/10.1073/pnas.2200514119.

Klein, S. A., and D. L. Hartmann, 1993: The seasonal cycle of low stratiform clouds. *J. Climate*, **6**, 1587–1606, https://doi.org/10.1175/1520-0442(1993)006⟨1587:TSCOLS⟩2.0.CO;2.

Kosaka, Y., and S.-P. Xie, 2013: Recent global-warming hiatus tied to equatorial Pacific surface cooling. *Nature*, **501**, 403–407, https://doi.org/10.1038/nature12534.

Larson, S. M., K. McMonigal, Y. Okumura, D. Amaya, A. Capotondi, K. Bellomo, I. R. Simpson, and A. C. Clement, 2024: Ocean complexity shapes sea surface temperature variability in a CESM2 coupled model hierarchy. *J. Climate*, **37**, 4931–4948, https://doi.org/10.1175/JCLI-D-23-0621.1.

Loeb, N. G., S.-H. Ham, R. P. Allan, T. J. Thorsen, B. Meyssignac, S. Kato, G. C. Johnson, and J. M. Lyman, 2024: Observational assessment of changes in Earth's energy imbalance since 2000. *Surv. Geophys.*, **45**, 1757–1783, https://doi.org/10.1007/s10712-024-09838-8.

Loeb, N. G., and Coauthors, 2018: Clouds and the Earth's Radiant Energy System (CERES) Energy Balanced and Filled (EBAF) Top-of-Atmosphere (TOA) Edition-4.0 data product. *J. Climate*, **31**, 895–918, https://doi.org/10.1175/JCLI-D-17-0208.1.

Luongo, M. T., S.-P. Xie, I. Eisenman, S. Sun, and Q. Peng, 2025: How the subsurface tropical Pacific responds to subtropical surface cooling: Implications for cross-equatorial transport. *J. Climate*, **38**, 3313–3331, https://doi.org/10.1175/JCLI-D-24-0440.1.

Lutsko, N. J., and K. Takahashi, 2018: What can the internal variability of CMIP5 models tell us about their climate sensitivity? *J. Climate*, **31**, 5051–5069, https://doi.org/10.1175/JCLI-D-17-0736.1.

Metz, W., 1991: Optimal relationship of large-scale flow patterns and the barotropic feedback due to high-frequency eddies. *J. Atmos. Sci.*, **48**, 1141–1159, https://doi.org/10.1175/1520-0469(1991)048⟨1141:OROLSF⟩2.0.CO;2.

Miyamoto, A., H. Nakamura, and T. Miyasaka, 2018: Influence of the subtropical high and storm track on low-cloud fraction and its seasonality over the south Indian Ocean. *J. Climate*, **31**, 4017–4039, https://doi.org/10.1175/JCLI-D-17-0229.1.

Miyamoto, A., H. Nakamura, T. Miyasaka, and Y. Kosaka, 2021: Radiative impacts of low-level clouds on the summertime subtropical high in the south Indian Ocean simulated in a coupled general circulation model. *J. Climate*, **34**, 3991–4007, https://doi.org/10.1175/JCLI-D-20-0709.1.

Miyamoto, A., H. Nakamura, S.-P. Xie, T. Miyasaka, and Y. Kosaka, 2023: Radiative impacts of Californian marine low clouds on North Pacific climate in a global climate model. *J. Climate*, **36**, 8443–8459, https://doi.org/10.1175/JCLI-D-23-0153.1.

Miyamoto, A., and S.-P. Xie, 2025: Low cloud-SST variability over the summertime subtropical northeast Pacific: Role of extratropical atmospheric modes. *J. Climate*, **38**, 165–180, https://doi.org/10.1175/JCLI-D-24-0015.1.

Myers, T. A., R. C. Scott, M. D. Zelinka, S. A. Klein, J. R. Norris, and P. M. Caldwell, 2021: Observational constraints on low cloud feedback reduce uncertainty of climate sensitivity. *Nat. Climate Change*, **11**, 501–507, https://doi.org/10.1038/s41558-021-01039-0.

Okumura, Y. M., 2013: Origins of tropical Pacific decadal variability: Role of stochastic atmospheric forcing from the South Pacific. *J. Climate*, **26**, 9791–9796, https://doi.org/10.1175/JCLI-D-13-00448.1.

Olonscheck, D., and M. Rugenstein, 2024: Coupled climate models systematically underestimate radiation response to surface warming. *Geophys. Res. Lett.*, **51**, e2023GL106909, https://doi.org/10.1029/2023GL106909.

Platnick, S., M. D. King, S. A. Ackerman, W. P. Menzel, B. A. Baum, J. C. Riedi, and R. A. Frey, 2003: The MODIS cloud products: Algorithms and examples from Terra. *IEEE Trans. Geosci. Remote Sens.*, **41**, 459–473, https://doi.org/10.1109/TGRS.2002.808301.

Proistosescu, C., A. Donohoe, K. C. Armour, G. H. Roe, M. F. Stuecker, and C. M. Bitz, 2018: Radiative feedbacks from stochastic variability in surface temperature and radiative imbalance. *Geophys. Res. Lett.*, **45**, 5082–5094, https://doi.org/10.1029/2018GL077678.

Raghuraman, S. P., D. Paynter, and V. Ramaswamy, 2021: Anthropogenic forcing and response yield observed positive trend in Earth's energy imbalance. *Nat. Commun.*, **12**, 4577, https://doi.org/10.1038/s41467-021-24544-4.

Rugenstein, M., M. Zelinka, K. B. Karnauskas, P. Ceppi, and T. Andrews, 2023: Patterns of surface warming matter for climate sensitivity. *Eos*, 104, https://doi.org/10.1029/2023EO230411.

Senior, C. A., and J. F. B. Mitchell, 2000: The time-dependence of climate sensitivity. *Geophys. Res. Lett.*, **27**, 2685–2688, https://doi.org/10.1029/2000GL011373.

606 Sherwood, S. C., and Coauthors, 2020: An assessment of Earth's climate sensitivity using multiple
607 lines of evidence. *Rev. Geophys.*, **58**, e2019RG000678, https://doi.org/10.1029/2019RG000678.

608 Small, R. J., S.-P. Xie, Y. Wang, S. K. Esbensen, and D. Vickers, 2005: Numerical simulation
609 of boundary layer structure and cross-equatorial flow in the eastern Pacific. *J. Atmos. Sci.*, **62**,
610 1812–1830, https://doi.org/10.1175/JAS3433.1.

611 Sobel, A. H., J. Nilsson, and L. M. Polvani, 2001: The weak temperature gradient approximation
612 and balanced tropical moisture waves. *J. Atmos. Sci.*, **58**, 3650–3665, https://doi.org/10.1175/
613 1520-0469(2001)058⟨3650:TWTGAA⟩2.0.CO;2.

614 Sun, T., and Y. M. Okumura, 2019: Role of stochastic atmospheric forcing from the South and
615 North Pacific in tropical Pacific decadal variability. *J. Climate*, **32**, 4013–4038, https://doi.org/
616 10.1175/JCLI-D-18-0536.1.

617 Tsuchida, K., Y. Kosaka, and S. Minobe, 2026: Multi-year La Niña-El Niño transition in-
618 fluenced Earth's extreme energy uptake in 2022-2023. *Nat. Geosci.*, https://doi.org/10.1038/
619 s41561-026-01921-6.

620 Tsuchida, K., T. Mochizuki, R. Kawamura, T. Kawano, and Y. Kamae, 2023: Diversity of lagged
621 relationships in global means of surface temperatures and radiative budgets for CMIP6 piControl
622 simulations. *J. Climate*, **36**, 8743–8759, https://doi.org/10.1175/JCLI-D-23-0045.1.

623 Vimont, D. J., 2005: The contribution of the interannual ENSO cycle to the spatial pattern of
624 decadal ENSO-like variability. *J. Climate*, **18**, 2080–2092, https://doi.org/10.1175/JCLI3365.1.

625 Vimont, D. J., M. A. Alexander, and M. Newman, 2014: Optimal growth of Central and East Pacific
626 ENSO events. *Geophys. Res. Lett.*, **41**, 4027–4034, https://doi.org/10.1002/2014GL059997.

627 Wills, R. C. J., K. C. Armour, D. S. Battisti, C. Proistosescu, and L. A. Parsons, 2021: Slow modes
628 of global temperature variability and their impact on climate sensitivity estimates. *J. Climate*,
629 **34**, 8717–8738, https://doi.org/10.1175/JCLI-D-20-1013.1.

630 Wood, R., and C. S. Bretherton, 2006: On the relationship between stratiform low cloud cover and
631 lower-tropospheric stability. *J. Climate*, **19**, 6425–6432, https://doi.org/10.1175/JCLI3988.1.

Xie, S.-P., C. Deser, G. A. Vecchi, J. Ma, H. Teng, and A. T. Wittenberg, 2010: Global warming pattern formation: Sea surface temperature and rainfall. *J. Climate*, **23**, 966–986, https://doi.org/10.1175/2009JCLI3329.1.

Xie, S.-P., K. Hu, J. Hafner, H. Tokinaga, Y. Du, G. Huang, and T. Sampe, 2009: Indian Ocean capacitor effect on Indo-Western Pacific climate during the summer following El Niño. *J. Climate*, **22**, 730–747, https://doi.org/10.1175/2008JCLI2544.1.

Xie, S.-P., Y. Kosaka, and Y. M. Okumura, 2016: Distinct energy budgets for anthropogenic and natural change during global warming hiatus. *Nat. Geosci.*, **9**, 29–33, https://doi.org/10.1038/ngeo2581.

Xie, S.-P., and S. G. H. Philander, 1994: A coupled ocean-atmosphere model of relevance to the ITCZ in the eastern Pacific. *Tellus*, **46A**, 340–350, https://doi.org/10.3402/tellusa.v46i4.15484.

Yang, L., S.-P. Xie, S. S. P. Shen, J.-W. Liu, and Y.-T. Hwang, 2023: Low cloud-SST feedback over the subtropical Northeast Pacific and the remote effect on ENSO variability. *J. Climate*, **36**, 441–452, https://doi.org/10.1175/JCLI-D-21-0902.1.

Zelinka, M. D., T. A. Myers, D. T. McCoy, S. Po-Chedley, P. M. Caldwell, and P. Ceppi, 2020: Causes of higher climate sensitivity in CMIP6 models. *Geophys. Res. Lett.*, **47**, e2019GL085782, https://doi.org/10.1002/2015GL067416.

Zhang, H., A. Clement, and P. Di Nezio, 2014: The South Pacific meridional mode: A mechanism for ENSO-like variability. *J. Climate*, **27**, 769–783, https://doi.org/10.1175/JCLI-D-13-00082.1.

Zhao, M., and Coauthors, 2018: The GFDL global atmosphere and land model AM4.0/LM4.0: 1. Simulation characteristics with prescribed SSTs. *J. Adv. Model. Earth Syst.*, **10**, 691–734, https://doi.org/10.1002/2017MS001208.

Zhou, C., M. D. Zelinka, and S. A. Klein, 2016: Impact of decadal cloud variations on the Earth's energy budget. *Nat. Geosci.*, **9**, 871–874, https://doi.org/10.1038/ngeo2828.

Zhou, C., M. D. Zelinka, and S. A. Klein, 2017: Analyzing the dependence of global cloud feedback on the spatial pattern of sea surface temperature change with a Green's function approach. *J. Adv. Model. Earth Syst.*, **9**, 2174–2189, https://doi.org/10.1002/2017MS001096.